

Improving seismic fault detection by super-attribute-based classification

Haibin Di¹, Mohammad Amir Shafiq², Zhen Wang², and Ghassan AlRegib²

Abstract

Fault interpretation is one of the routine processes used for subsurface structure mapping and reservoir characterization from 3D seismic data. Various techniques have been developed for computer-aided fault imaging in the past few decades; for example, the conventional methods of edge detection, curvature analysis, red-green-blue rendering, and the popular machine-learning methods such as the support vector machine (SVM), the multilayer perceptron (MLP), and the convolutional neural network (CNN). However, most of the conventional methods are performed at the sample level with the local reflection pattern ignored and are correspondingly sensitive to the coherent noises/processing artifacts present in seismic signals. The CNN has proven its efficiency in utilizing such local seismic patterns to assist seismic fault interpretation, but it is quite computationally intensive and often demands higher hardware configuration (e.g., graphics processing unit). We have developed an innovative scheme for improving seismic fault detection by integrating the computationally efficient SVM/MLP classification algorithms with local seismic attribute patterns, here denoted as the super-attribute-based classification. Its added values are verified through applications to the 3D seismic data set over the Great South Basin (GSB) in New Zealand, where the subsurface structure is dominated by polygonal faults. A good match is observed between the original seismic images and the detected lineaments, and the generated fault volume is tested usable to the existing advanced fault interpretation tools/modules, such as seeded picking and automatic extraction. It is concluded that the improved performance of our scheme results from its two components. First, the SVM/MLP classifier is computationally efficient in parsing as many seismic attributes as specified by interpreters and maximizing the contributions from each attribute, which helps minimize the negative effects from using a less useful or “wrong” attribute. Second, the use of super attributes incorporates local seismic patterns into training a fault classifier, which helps exclude the random noises and/or artifacts of distinct reflection patterns.

Introduction

Faults and fractures are important subsurface structures of significant geologic implications for hydrocarbon accumulation and migration in a petroleum reservoir, and the presence of a fault can be visually recognized as a lineament/plane of abrupt variations of the reflection signals in a 3D seismic data set. However, fault interpretation is a time-consuming and labor-intensive process, especially for an exploration area of a large number of faults and complicated faulting histories and distributions. In the past few decades, great efforts have been devoted into computer-aided fault interpretation by developing new attributes and methods/algorithms to help detect, depict, and extract the faults of interpretational interest from the surrounding nonfaulting features.

Specifically, from the perspective of seismic attribute analysis, edge detection and reflector geometry estimation are applicable to the problem of fault mapping

from 3D seismic data, owing to the lateral changes in seismic signals across a fault, including reflection waveform/amplitude and depth/two-way traveltime. Geoscientists have devoted substantial efforts for quantifying such changes and improving the resolution and noise robustness of fault detection (e.g., [Bahorich and Farmer, 1995](#); [Luo et al., 1996](#); [Marfurt et al., 1998](#); [Gersztenkorn and Marfurt, 1999](#); [van Bemmelen and Pepper, 2000](#); [Cohen and Coifman, 2002](#); [Tingdahl and de Rooij, 2005](#); [Di and Gao, 2014a](#); [Wang et al., 2016](#)). For example, [Bahorich and Farmer \(1995\)](#) present the coherence attribute by estimating the crosscorrelation of two adjacent seismic traces to highlight the faults and stratigraphic features from a seismic cube. [Marfurt et al. \(1998\)](#) present the semblance attribute by estimating the amplitude variations in a horizontal window. [Gersztenkorn and Marfurt \(1999\)](#) perform principal component analysis on a local coherence cube for

¹Formerly Georgia Institute of Technology, School of Electrical and Computer Engineering, Center for Energy and Geo Processing (CeGP), Atlanta, Georgia 30308, USA; presently Schlumberger, Houston, Texas 77056, USA. E-mail: hdi7@gatech.edu.

²Georgia Institute of Technology, School of Electrical and Computer Engineering, Center for Energy and Geo Processing (CeGP), Atlanta, Georgia 30308, USA. E-mail: amirshafiq@gatech.edu; zwang313@gatech.edu; alregib@gatech.edu.

Manuscript received by the Editor 18 October 2018; revised manuscript received 4 February 2019; published ahead of production 03 June 2019; published online 7 August 2019. This paper appears in *Interpretation*, Vol. 7, No. 3 (August 2019); p. SE251–SE267, 18 FIGS., 13 TABLES.

<http://dx.doi.org/10.1190/INT-2018-0188.1>. © 2019 Society of Exploration Geophysicists and American Association of Petroleum Geologists. All rights reserved.

improved coherence analysis. [Cohen and Coifman \(2002\)](#) propose using the local structural entropy for fault mapping. [Tingdahl and de Rooij \(2005\)](#) develop the similarity operator for measuring the differences between two seismic trace segments. [Di and Gao \(2014a\)](#) compare the performance of the common edge detectors, including the popular Canny detector, on seismic fault detection. A comprehensive summary of the edge-detection attributes can be found in [Chopra \(2002\)](#), [Kington \(2015\)](#), and [Di and Gao \(2017a\)](#). However, the conventional seismic edge detection is limited in its detection resolution for small-scale faults and fractures beyond the seismic scale and offers no physical link for predicting the fundamental fracture properties (e.g., intensity, orientation, and sense of displacement) either quantitatively or qualitatively ([Gao, 2013](#)). Then, the seismic geometric attributes are developed for more robust fault detection and fracture characterization by quantifying the lateral variations of the geometry of seismic reflectors, including the first-order dip, the second-order curvature, and the third-order flexure attributes. Specifically, the dip describes the local dipping of a reflector, and a fault is highlighted as a lineament of large dipping angle. The curvature describes the bending of a reflector, and a fault is highlighted as a juxtaposition of positive and negative curvatures ([Roberts, 2001](#); [Al-Dossary and Marfurt, 2006](#)). The flexure describes the shearing of a reflector, and a fault is highlighted as a local peak accompanied with two subtle side lobes ([Gao, 2013](#); [Di and Gao, 2014b, 2016a, 2016b](#); [Yu, 2014](#); [Gao and Di, 2015](#); [Qi and Marfurt, 2018](#)). Comprehensive summaries of the curvature and flexure analysis can be found in [Roberts \(2001\)](#) and [Di and Gao \(2017b\)](#), respectively.

From the perspective of fault-interpretation methods, manual picking is considered most reliable if performed by an experienced interpreter. However, it is limited by the interpretation efficiency especially for a large seismic data set with a complicated deformation history (e.g., folding and faulting). Correspondingly, computer-aided fault interpretation becomes the research focus with the progress in computer graphics and image processing since 2000, and various methods/algorithms have been developed for refining the edge-detection attributes and interpreting fault surfaces (e.g., [Crawford and Medwedeff, 1999](#); [Pedersen et al., 2002](#); [Admasu et al., 2006](#); [Barnes, 2006](#); [Lavialle et al., 2007](#); [Hale, 2013](#); [Zhang et al., 2014](#); [Machado et al., 2016](#); [Wu and Hale, 2016](#); [Wu and Fomel, 2018](#); [Di and AlRegib, 2019](#)). For example, [Pedersen et al. \(2002\)](#) introduce the concept of ant colony optimization from computer science and develop an ant-tracking algorithm for sharpening the lineaments in a variance volume. [AlBinHassan and Marfurt \(2003\)](#) apply the 2D Hough transform for enhancing the fault lines on time slices; later, [Wang and AlRegib \(2014\)](#) extend it to 3D space for fault surface extraction from a semblance volume. [Barnes \(2006\)](#) performs eigenvector analysis to a coherence volume and designs a discontinuity filter of three components for imaging the steeply dipping faults.

[Admasu et al. \(2006\)](#) propose an autotracking method of fault line propagation from one vertical section to another throughout a seismic volume for extracting an individual fault patch. [Lavialle et al. \(2007\)](#) present a nonlinear filtering approach for noise suppression and fault enhancement based on 3D gradient structure tensor analysis. [Hale \(2013\)](#) proposes scanning over all possible fault orientations for computing fault likelihood (fault-oriented semblance), strikes, and dips, constructing fault surfaces as quad meshes from the three fault images, and further applying a dynamic time warping algorithm to estimate fault throws on the each fault surface. [Zhang et al. \(2014\)](#) first apply a biometric algorithm to the coherence attribute for fault skeletonization and then group discrete fault points into one fault patch under local planar constraints ([Gibson et al., 2005](#)). [Wang et al. \(2014a\)](#) borrow the ideas of motion vectors in video coding and processing to assist seismic fault extraction. [Machado et al. \(2016\)](#) perform volumetric fault imaging (VFI) by applying the directional Laplacian of a Gaussian filter to coherence anomalies along reflector dip and azimuth. [Wu and Hale \(2016\)](#) propose using the fault skin, a simple linked-data structure, to construct fault surfaces and fill holes. [Wu and Fomel \(2018\)](#) present an optimal surface voting algorithm to enhance a fault attribute image, estimate fault orientations, and construct complete fault surfaces. [Di and AlRegib \(2019\)](#) propose computing fault probability from seismic geometric faults and picking faults based on one or more seeds specified by interpreters.

If examined from the perspective of their inputs, most of these methods use only a single edge-detection attribute (e.g., semblance, coherence, and variance), implying their full dependency on the attribute quality. In geology, however, some nonfault features (e.g., salt domes and stratigraphic channels), coherent noises (e.g., acquisition footprints), and processing artifacts are often detectable by a certain edge-detection algorithm and correspondingly would interfere the interpretation of actual faults if such an attribute is feed into computer-aided fault interpretation ([Ashbridge et al., 2000](#); [Barnes, 2006](#)). The risk can be reduced by integrating multiple seismic attributes of distinct operators, such as coherence and curvature. One simple approach is through a visualization of several attributes at a time, such as the corendering of three attributes in the red-green-blue (RGB) or hue-saturation-value color space (e.g., [Partyka et al., 1999](#); [Dorn, 2002](#); [Stark, 2006](#); [Laake, 2013](#); [Wang et al., 2014b](#)). But such visualization is limited to the capability of our human vision system, and it is usually difficult to capture and parse more than five attributes. An alternative approach is to integrate multiple attribute through artificial intelligence, such as with the multilayer perceptron (MLP) ([Tingdahl and de Rooij, 2005](#); [Odoh et al., 2014](#); [Zheng et al., 2014](#)) and the support vector machine (SVM) ([Di et al., 2017](#)). To the best of our knowledge, such multiattribute analysis is often based on the attribute values at each seismic sample, without taking into account the local seismic patterns, causing its limited

capability of differentiating seismic noises from true faults, when they share similar attribute values but appear visually distinct from the perspective of reflection patterns. For better noise robustness, the emerging convolutional neural network (CNN) has been implemented for seismic fault detection directly from the original amplitude (Huang et al., 2017; Di et al., 2018a; Lu et al., 2018; Xiong et al., 2018; Zhao and Mukhopadhyay, 2018; Wu et al., 2019). The contribution of using local seismic patterns has been investigated by Di et al. (2018b). Meanwhile, the CNN is observed more computationally expensive in terms of hardware and processing time compared with SVM/MLP schemes.

In this paper, we propose an innovative workflow for improved fault detection by integrating the efficient SVM/MLP classifiers and local seismic attribute patterns, here denoted as the super-attribute-based classification (SAC). The paper is organized as follows. We first illustrated the proposed SAC scheme in detail. Then, we demonstrate its added values through applications to the 3D seismic data set over the Great South Basin (GSB) in New Zealand, where polygonal faulting dominates the subsurface structures. Then, we discuss the potential of further improvement by 3D super-attribute retrieval and CNN-based automatic seismic attribute extraction. Finally, we draw our conclusions at the end.

Algorithm description

Figure 1 illustrates the proposed SAC workflow for improving fault detection from 3D seismic data. It consists of five steps: (1) attribute selection, (2) training sample labeling, (3) super-attribute retrieval, (4) machine learning (ML) classifier training and evaluation, and (5) volumetric processing. A detailed description of each step is provided below. For efficient evaluation of the proposed workflow, we use a small subset of the 3D seismic data set of 484 inlines by 501 crosslines by 76 samples per trace over the GSB in New Zealand, where the subsurface structure is featured with polygonal faulting. Figure 2 displays the time section at 1132 ms of the original seismic amplitude, in which we can easily recognize a number of faults of varying ori-

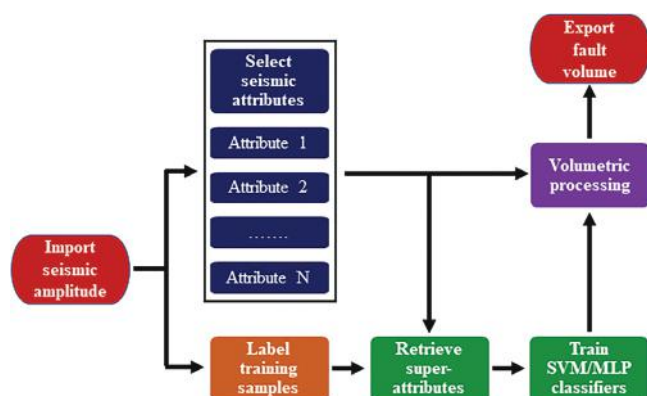


Figure 1. The workflow chart of the proposed super-attribute-based SVM/MLP classification for improving fault detection from 3D seismic data.

entations that break the reflection continuity. The workflow is performed on the entire seismic volume, and for the convenience of result illustration and comparison in this paper, we clip the output volume of every step to 2D sections and display them in the corresponding figures.

Attribute selection

Attribute selection is considered as the key to successful multiattribute-based seismic feature classification, such as facies analysis (Barnes and Laughlin, 2002; Zhao et al., 2015) and salt body delineation (Di et al., 2018c). For fault interpretation in this study, we determine an attribute useful by visually verifying whether the faults can be visually differentiated from the surrounding nonfaulting features (such as horizons) in the corresponding attribute map. Among all possible seismic attributes, we select and calculate 14 attributes from the amplitude volume (Table 1), which are categorized into three groups:

- 1) Geometric attributes: The group of seismic geometric attribute measures the lateral changes in the geometry of seismic reflectors in different scales, including the first-order dip, the second-order curvature (Roberts, 2001), the third-order flexure (Di and Gao, 2017a), and the geometric fault probability (GFP) (Di and AlRegib, 2017, 2019). As shown in Figure 3, each of the geometric attributes highlights the faults in its unique expression. Specifically, a fault is recognized as a lineament of a large dipping angle (Figure 3a), a juxtaposition of positive and negative curvatures (Figure 3b), peak flexure with two subtle side lobes (Figure 3c), and peak GFP (Figure 3d).

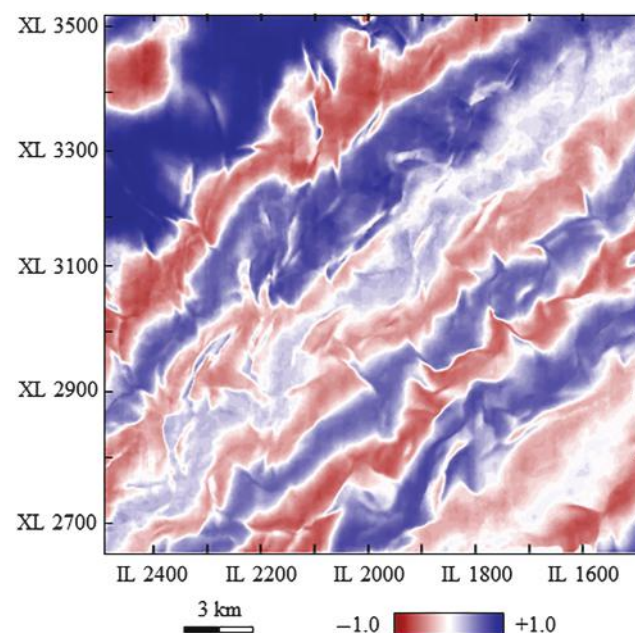


Figure 2. The time slice of original seismic amplitude at 1132 ms over the GSB in New Zealand, where the structure is dominated by polygonal faulting.

- 2) Edge-detection attributes: The group of seismic edge-detection attributes evaluates the lateral changes in the seismic waveform and/or amplitude using various mathematical operators, including coherence (Bahorich and Farmer, 1995), Sobel filtering (Luo et al., 1996), semblance (Marfurt et al., 1998), Canny edge detection (Di and Gao, 2014a), similarity (Tingdahl and de Rooij, 2005), and variance (van Bemmelen and Pepper, 2000). As shown in Figure 4, a fault is recognized as a lineament of low coherence (Figure 4a), high Sobel (Figure 4b), low semblance (Figure 4c), high Canny (Figure 4d), low similarity (Figure 4e), and high variance (Figure 4f).
- 3) Texture attributes: The group of seismic texture attributes describes the local distribution of seismic texture in various statistical ways, including gray-level cooccurrence matrix (GLCM) contrast and homogeneity (Gao, 2003; Eichkitz et al., 2013; Di and Gao, 2017c), gradient of texture (GOT) (Shafiq et al., 2015), and seismic saliency (Shafiq et al., 2016). Such an attribute group is often applied for seismic facies analysis; however, considering the apparent lateral changes in seismic signals distorted by faults, these texture attributes are found to

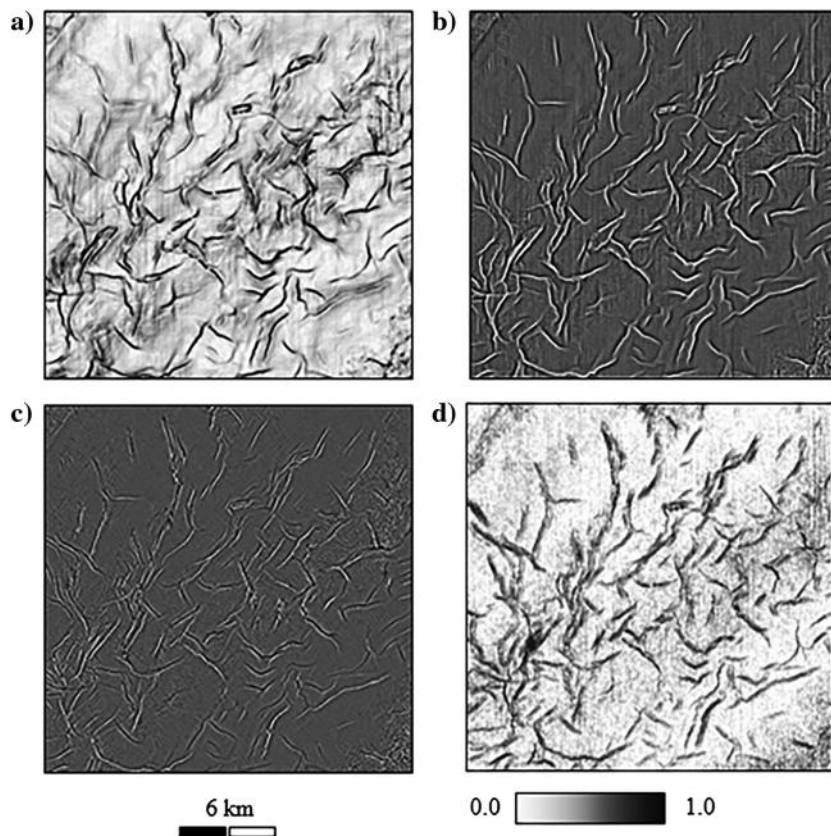


Figure 3. The group of geometric attributes used for the proposed super-attribute-based fault detection from 3D seismic data, including (a) reflector dip, (b) curvature, (c) flexure, and (d) GFP. All attributes are normalized for visualization and classification.

Table 1. The manually selected 14 seismic attributes used for the proposed seismic fault detection via super-attribute-based SVM/MLP classification.

Group	Attribute	Measurement	Fault indicator
Geometric attribute	Dip	Lateral changes of seismic reflector geometry at various scales	Local maximum
	Curvature		Local maximum and minimum
	Flexure		Local maximum or minimum
	GFP		Local maximum
Edge-detection attribute	Coherence	Lateral changes in seismic waveform and/or amplitude by various math operators	Local minimum
	Sobel edge		Local maximum
	Semblance		Local minimum
	Canny edge		Local maximum
	Similarity		Local minimum
	Variance		Local maximum
Texture attribute	GLCM contrast	Statistical analysis of local seismic amplitude distribution	Local maximum
	GLCM homogeneity		Local minimum
	GOT	seismic texture variation	Local maximum
	Saliency	Attraction to interpreter eyes	Local maximum

be capable of highlighting the target faults in the GSB area. As shown in Figure 5, a fault lineament is of high GLCM contrast (Figure 5a), low GLCM homogeneity (Figure 5b), high GOT (Figure 5c), and high seismic saliency (Figure 5d).

Before feeding these attributes into the ML classification, we observe different units of measurement and moreover distinct histograms between the selected 14 attributes. For example, the contrast of the GOT attribute between the target faults and nonfaulting features is relatively smaller than the GLCM attributes, and the seismic saliency attribute has a lower mean value compared with the edge-detection attributes. For avoiding the shadow effects from the “strong” attributes of a large mean and promoting the contribution from “insensitive” attributes of a small standard deviation, each of the selected 14 attributes is normalized to be between 0.0 and 1.0 in this work, not only for visual comparisons in Figures 3–5, but more importantly to balance the sensitivity of a fault/non-fault sample to various attributes in the 14D attribute domain.

Training sample labeling

Reliable training data are essential for accurate supervised classification. Due to the lack of common training data sets in the field of seismic interpretation, we prepare the training samples used in this work by manually labeling the faults observed in three vertical sections of cross-line 2790, 2800, and 2810 (Figure 6), which provides us with approximately 6000 fault labels and 100,000 nonfault labels. The training labels serve for the proposed workflow in two ways. First, attribute crossplotting over both labels makes it possible for verifying the quality and capability of the selected 14 attributes in differentiating faults and non-faults in the given data set. Ideally, the two labels are expected to be well-separated into two groups with no or little overlapping. However, due to the presence of seismic noise (e.g., acquisition footprint), no attribute is yet found to serve well for the ideal case. Figure 7 displays the crossplotting of three attributes, including GLCM homogeneity versus variance and GLCM contrast versus variance, with the fault and nonfault labels denoted in green and blue, respectively. Apparently, the fault labels are grouped with high variance, low GLCM homogeneity, and high GLCM contrast, which is consistent with the fault indica-

tors summarized in Table 1. Meanwhile, the obvious overlapping indicates the limited capability of these attributes in fault differentiation and accounts for the misclassifications observed in the results (Figures 10, 11, 12, 13, 14, and 15 and Tables 3, 4, 5, 6, and 7).

Second, applying a trained ML classifier to the labeled section makes it possible for quickly verifying the classifier's capability before conducting classifier evaluation and volumetric processing that is computational expensive and time consuming. Ideally, the built classifier is expected capable of relabeling these pickings with 100% accuracy. However, for the overlapping points shown in Figure 7, the ML algorithms may have a limited capability

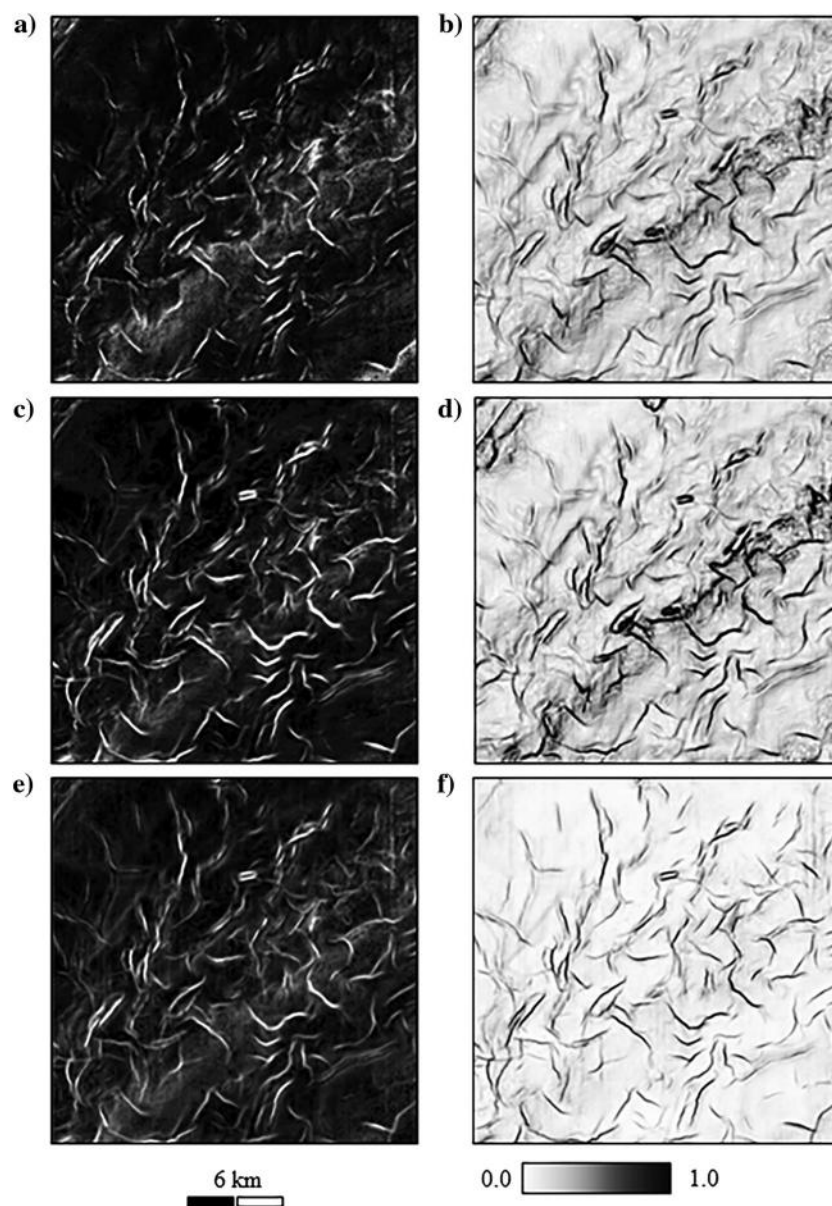


Figure 4. The group of edge-detection attributes used for the proposed super-attribute-based fault detection from 3D seismic data, including (a) coherence, (b) Sobel edge, (c) semblance, (d) Canny edge, (e) similarity, and (f) variance. All attributes are normalized for visualization and classification.

in identifying them from the provided 14 seismic attributes (Figures 3–5), and correspondingly misclassifications would occur (Figures 10–15 and Tables 3–7).

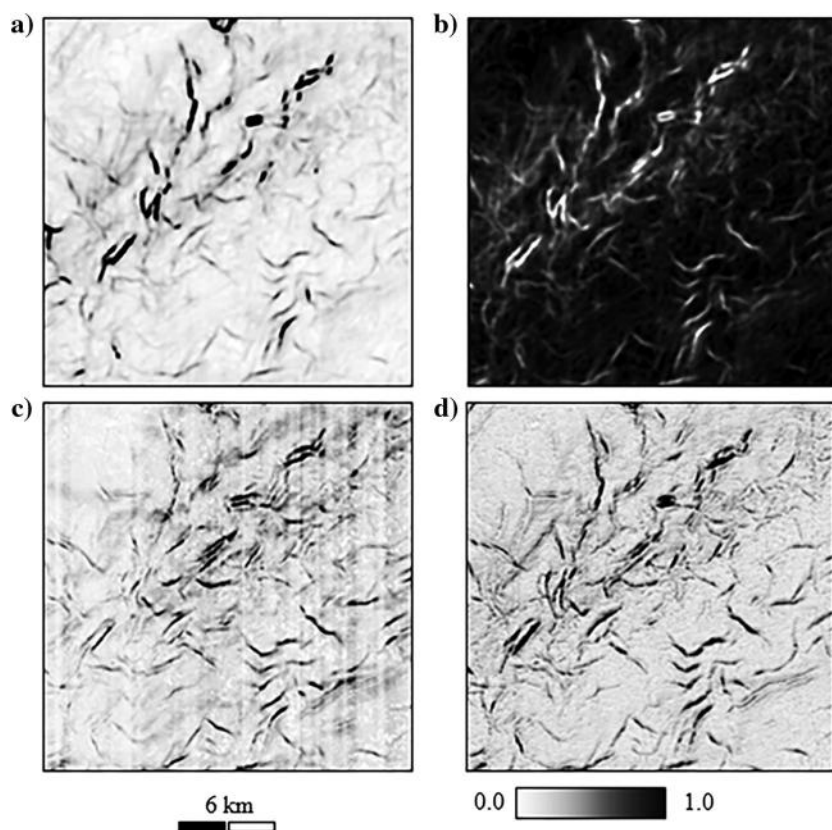


Figure 5. The group of texture attributes used for the proposed super-attribute-based fault detection from 3D seismic data, including (a) GLCM contrast, (b) GLCM homogeneity, (c) GOT, and (d) seismic saliency. All attributes are normalized for visualization and classification.

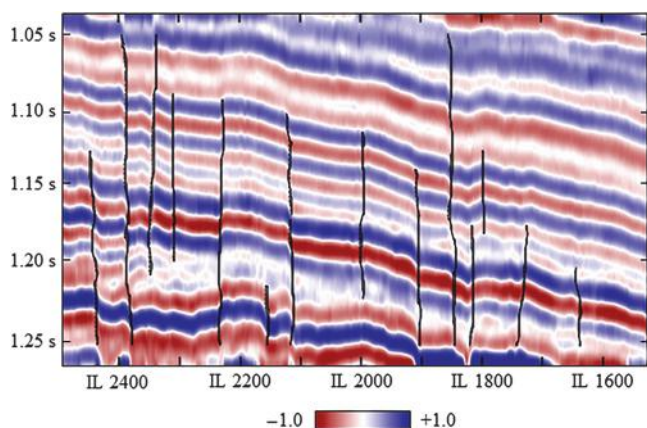


Figure 6. The manual pickings of the faults in the vertical section of crossline 2800 (denoted as the black lineaments), which are used as training samples for building an optimal SVM/MLP model.

Super-attribute retrieval

One major innovation of the proposed scheme over the traditional ones is to retrieve super attribute centered at every training sample, so that the ML algorithm learns the local attribute pattern at a sample, instead of

the signal attribute value. For the sole purpose of illustrating the feasibility of using a local seismic pattern to help seismic feature differentiation, we take acquisition footprints and seismic faults for example. Both are highlighted as lineaments of low coherency in a coherency map; therefore, it is difficult to differentiate them based only on the coherence value at each sample. However, if comparing them from the perspective of coherence pattern, they become distinguishable, with the acquisition footprints being straight in horizontal sections and propagating through vertical sections in 90° , whereas the faults are slightly curved in horizontal sections and cutting vertical sections in high angles (but not 90°). Therefore, pattern-based classification has the potential for promoting the differentiation of the true faults from the random noises, acquisition footprints, and processing artifacts. Figure 10 displays the detection of the faults in the vertical section of crossline 2800 using the proposed super-attribute-based scheme and the traditional sample-based scheme. It is clear that incorporating the local patterns into ML helps reduce the chance of mislabeling noises as faults (denoted as the circles in Figure 10c and 10d). The retrieval window used in this work is 9 inlines by 8 ms.

Classifier training and evaluating

Among all ML techniques available in image processing (e.g., random forest and neural network), this study implements two most popular and efficient algorithms:

- 1) SVM: The SVM is a discriminative classifier and has been widely applied for data mining in various engineering and science disciplines (e.g., Cortes and Vapnik, 1995; Lee et al., 2004; Cuingnet et al., 2011; Barghout, 2015). In the SVM algorithm as summarized in Zhao et al. (2015), each observation in a given data set is treated as a n -dimensional vector, where n denotes the number of features available at the observation. The SVM classifier aims at finding an $(n-1)$ -dimensional hyperplane (or decision boundary) that optimally separates the observations into two or more classes, so that the distance from one class to another is maximized. For the convenience of description, Figure 8 illustrates the two-class

(binary) SVM classification based on two features, which consists of three steps. First, every observation in a given data set is transformed into a vector of n elements corresponding to the available features and ($n = 2$ in this case). Second, a plane is estimated in the feature domain, which has the smallest distance to the observations in the data set. Finally, for quantitative evaluation of the classification accuracy, these vectors closest to the optimal hyperplane at both sides of the decision boundary are denoted as the support vectors, and the corresponding hyperplanes parallel to the optimal hyperplane are denoted as the plus and minus planes, respectively. Figure 10a displays the corresponding fault detection of crossline 2800 by the proposed super-attribute-based SVM classification.

- 2) MLP: The MLP is a class of feedforward artificial neural network consisting of at least three layers. Figure 9 illustrates the typical architecture of the MLP network used for seismic feature classification, such as gas the chimney (Meldahl et al., 1999), facies analysis (Zhao et al., 2015), and fault detection (Tingdahl and de Rooij, 2005; Zheng et al., 2014). In particular, the input layer contains n neurons each of which represents one of the labelled training samples and is an array of the selected m seismic attributes. The output layer has two neurons: true and false, which represents the fault and nonfault for the specific purpose of fault detection in this study. The two layers are connected by q hidden layers, each of which contains p neurons. In math, each neuron in the hidden layer(s) and the output layer is represented by a pair of weight and bias, which is optimized through training, so that a best mapping relationship is constructed between the output labels and the selected seismic attributes. The MLP network used in this study has $q = 3$ hidden layers and $p = 32$ neurons in each layer. Similarly, we display the corresponding fault detection of crossline 2800 by the proposed super-attribute-based multi-attribute MLP classification in Figure 10b. Table 2 lists the contributions of the selected 14 seismic attributes in training the optimal MLP classifier. The variance, geometric fault, and GLCM contrast are assigned the maximum contribution indicating the good correlation between the three attributes and the faults.

After training the SVM and MLP classifiers, we then manually label 10 vertical sections as the testing data set for evaluating their performance, including crosslines 2600, 2700, 2800, 2900, 3000, 3100, 3200, 3300, 3400, and 3500. Note that among them, only 2800 was used during the training process. The corresponding

confusion matrices are listed in Tables 3 and 4, respectively. For a fair comparison, the traditional sample-based SVM/MLP scheme is also conducted through the same process, with the corresponding confusion matrices in Tables 5 and 6. From the prediction images (Figure 10) and the confusion matrices (Tables 3–6), we have three observations. First, neither of the SVM

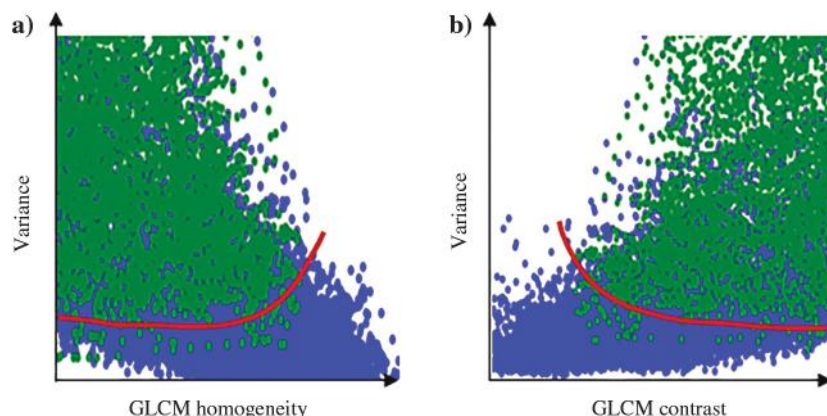


Figure 7. The crossplotting of the selected attribute on the manual pickings for verifying their capability in differentiating the faults of interpretational interest and the surrounding nonfaulting features. Take the (a) seismic saliency versus GLCM homogeneity and (b) geometric fault versus GLCM contrast for example. Such crossplotting demonstrates the clear border between the pickings on the fault (in green) and those on the nonfault features (in blue), which allows the classification of them into two separate groups.

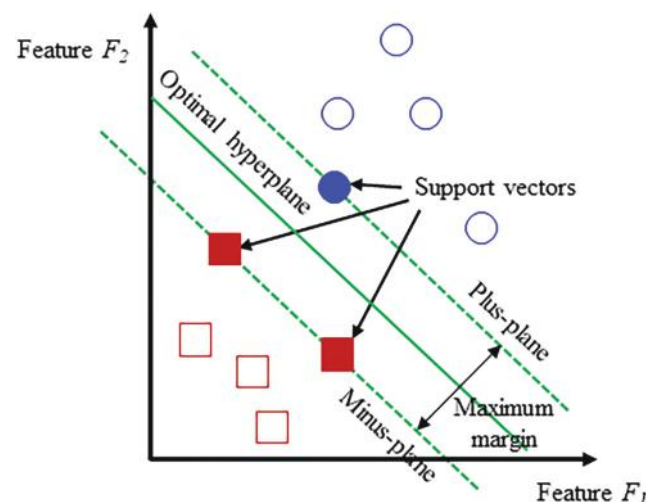


Figure 8. Sketch for illustrating the classification of 10 observations into two classes (denoted by the five blue circles and five red squares) by the SVM based on two features (modified from Zhao et al., 2015). The observations are represented by vectors in the feature domain, and a hyperplane (denoted as the solid green line) is found that optimally separates these observations. Those vectors closest to the hyperplane are often denoted as support vectors, and two associated hyperplanes parallel to the optimal one are denoted as plus and minus planes, respectively. The maximum margin is evaluated as the distance from the optimal hyperplane to the plus and minus planes.

nor MLP schemes accurately detected all the target faults, indicating their limited capability in classifying seismic features particularly in the overlapping samples shown in Figure 7. Second, the negative effects of seismic noises and nonfault features with distinct patterns are significantly eliminated by applying the proposed SAC scheme, as confirmed by the increased overall accuracy and reduced false-positive rate in the confusion matrix from the traditional sample-based schemes (Tables 5 and 6) to the proposed super-attribute-based schemes (Tables 3 and 4). Third, if comparing the SVM and MLP schemes, the MLP scheme leads to an overall higher detection accuracy than the SVM one, with more faults recognized (denoted by the rectangles in Figure 10b). Such improvement is consistent with the significant increasing of true position rate in the confusion matrix from 0.68 in the SVM scheme (Table 3) to 0.91 in the MLP scheme (Table 4). Meanwhile, we notice a slightly higher false-positive rate from the MLP scheme, which is corresponding to the thick lineaments observed in Figure 10.

Volumetric processing

After evaluating the accuracy of the built SVM and MLP classifiers, both are applied to the entire seismic survey for volumetric processing, providing us with fault volumes, in which the potential faults are highlighted in value 1.0. First, Figure 11 demonstrates the 3D view of the fault volumes (in the black)

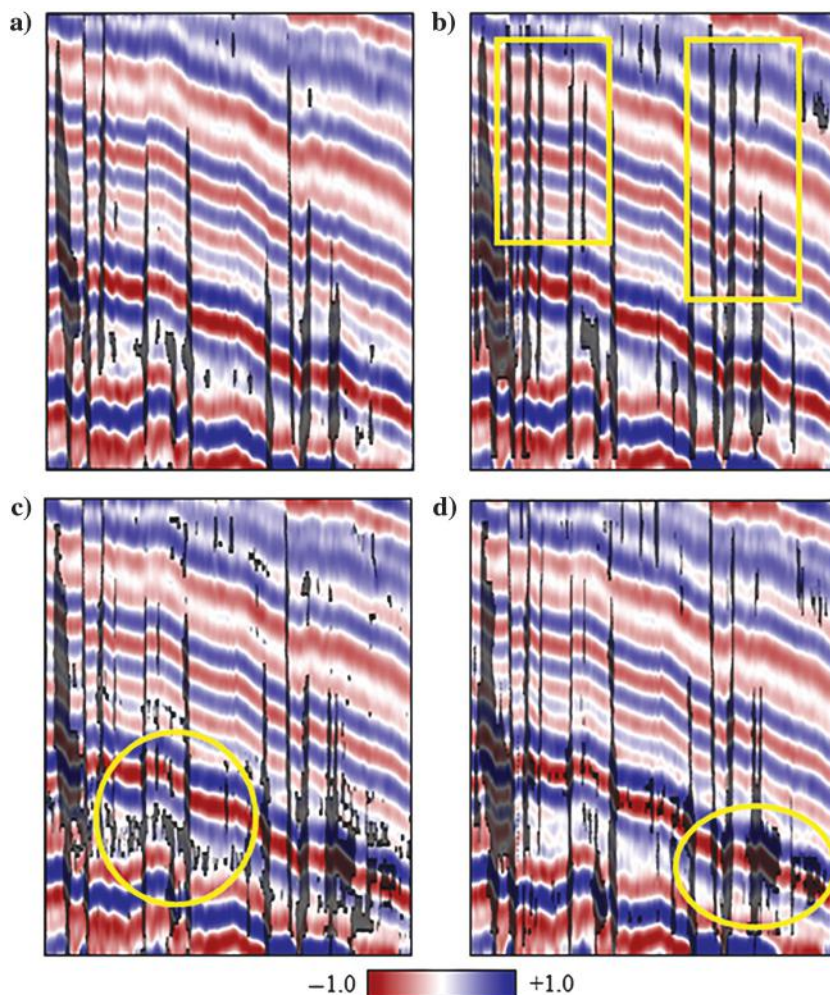


Figure 10. The reclassification of the manual pickings by the proposed super-attribute-based (a) SVM and (b) MLP classifiers compared with traditional sample-based (c) SVM and (d) MLP analysis, overlaying the vertical section of crossline 2800. Notice the improved visualization compared to the maps from the single samples.

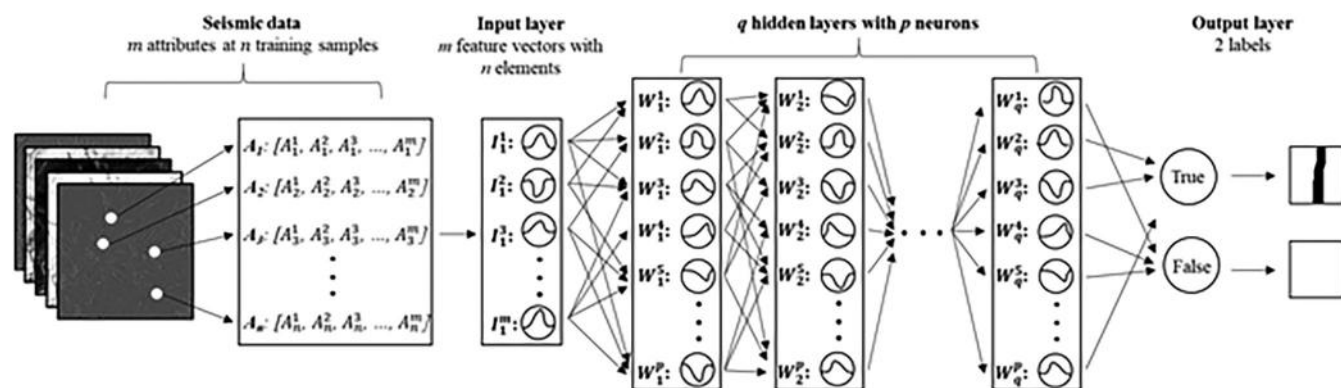


Figure 9. The diagram for illustrating the structure of the multiattribute-based MLP from 3D seismic data. The m attributes are retrieved at each of the n training samples that provides n neurons of the input layer, and the output layer consists of two labels, fault and nonfault. The input output layers are connected by q hidden layers, each of which contains p neurons. Such connection is optimized by adjusting the activities of all neurons, also known as weight w .

from the SVM and MLP schemes, overlaying the original seismic amplitude (in the blue-white-red). It is clear that both methods are capable of detecting the target faults,

Table 2. The contributions of the selected 14 seismic attributes in the trained optimal super-attribute-based MLP classifier.

Group	Attribute	Contribution (%)
Geometric attribute (weights = 25.56)	Dip	0.89
	Curvature	2.46
	Flexure	2.27
	GFP	19.94
Edge-detection attribute (weights = 56.07)	Coherence	0.43
	Sobel edge	0.56
	Semblance	0.07
	Canny edge	0.38
	Similarity	0.04
	Variance	54.59
	GLCM contrast	13.07
Texture attribute (weights = 18.37)	GLCM homogeneity	1.80
	GOT	0.60
	Saliency	2.90

Note: The variance contributes most, whereas the similarity is given least importance in determining the labels of the seismic samples.

Table 3. The confusion matrix of applying the proposed super-attribute-based SVM classification to the 10 testing sections.

		Prediction	
		Nonfault	Fault
Accuracy: 0.88			
True-positive rate: 0.68			
False-positive rate: 0.13			
Actual	Nonfault	271,480	42,448
	Fault	6074	12,718

Note the improved overall accuracy and reduced false-positive rate compared to the traditional sample-based SVM scheme (Table 5), which verifies the observations in Figure 10.

Table 4. The confusion matrix of applying the proposed super-attribute-based MLP classification to the 10 testing sections.

		Prediction	
Accuracy: 0.80			
True-positive rate: 0.91			
False-positive rate: 0.21		Nonfault	Fault
Actual	Nonfault	255,488	68,440
	Fault	1759	17,033

Note the improved overall accuracy and true-positive rate compared to the traditional sample-based scheme (Table 5) and improved true-positive rate compared to the super-attribute-based SVM scheme (Table 3), which verifies the observations in Figure 10.

particularly the MLP scheme as denoted by the circles in Figure 11b, which again verifies the better performance of the MLP scheme over the SVM scheme.

Then, we clip the MLP fault volume to the time section at 1132 ms (Figure 12) and four randomly selected vertical sections, including inline 1791, inline 2011,

Table 5. The confusion matrix of applying the traditional sample-based SVM classification to the 10 testing sections.

		Prediction	
Accuracy: 0.72			
True-positive rate: 0.77			
False-positive rate: 0.28		Nonfault	Fault
Actual	Nonfault	250,097	98,532
	Fault	4456	14,755

Table 6. The confusion matrix of applying the traditional sample-based MLP classification to the 10 testing sections.

		Prediction	
Accuracy: 0.75			
True-positive rate: 0.80			
False-positive rate: 0.25		Nonfault	Fault
Actual	Nonfault	261,257	87,372
	Fault	3760	15,451

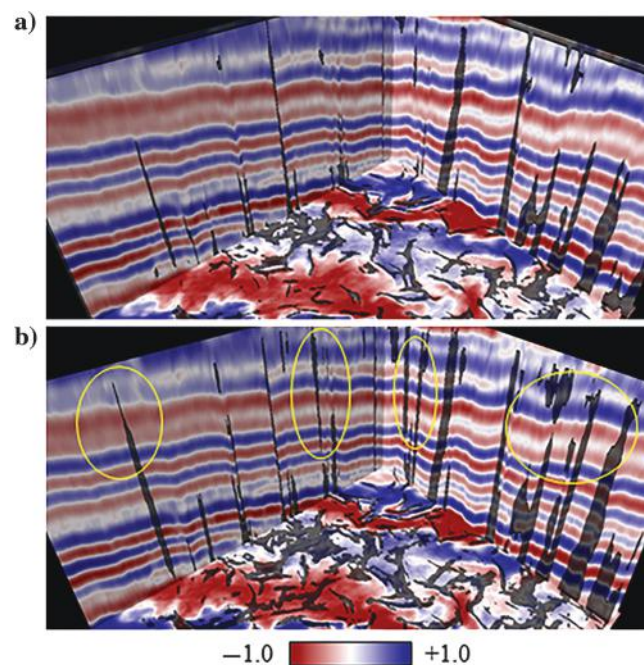


Figure 11. The 3D view of the detected faults in the GSB data set using the proposed super-attribute-based (a) SVM and (b) MLP classification. Note that noises are significantly reduced, and the faults are delineated more clearly (denoted as the circles).

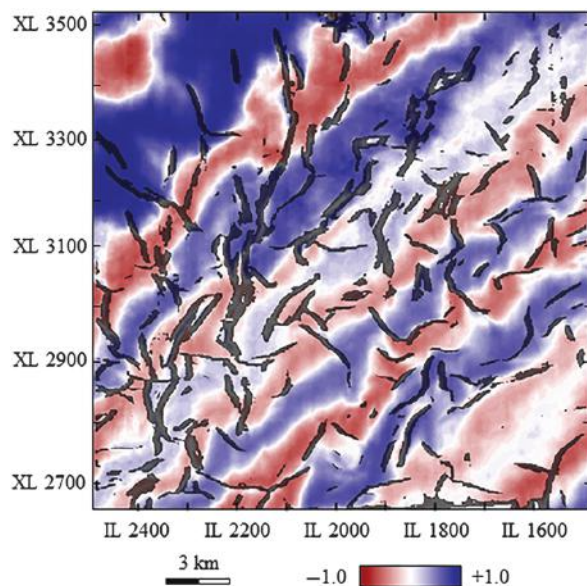


Figure 12. The detected fault lineaments overlaying the time section at 1132 ms using the proposed super-attribute-based MLP classification. Notice the improved visualization compared to the maps from the single samples (Figure 11).

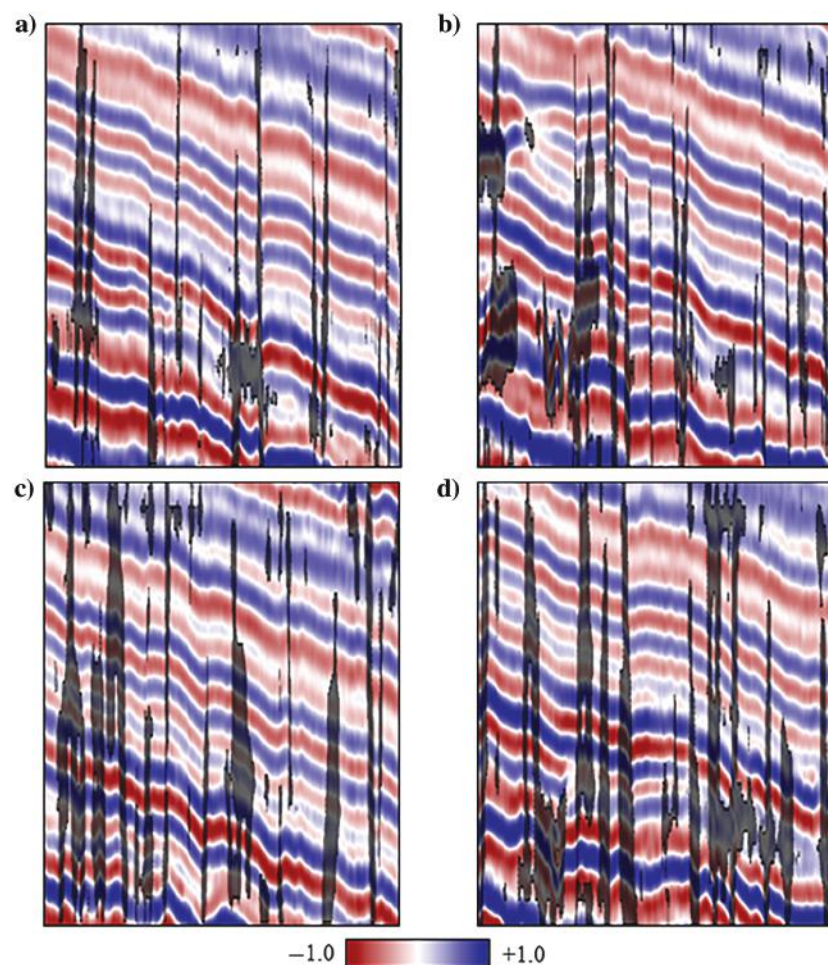


Figure 13. The clipping of the generated fault volume by the proposed super-attribute-based MLP classification to four randomly selected vertical sections, including (a) inline 1791, (b) inline 2011, (c) crossline 2600, and (d) crossline 3000.

crossline 2600, and crossline 3000 (Figure 13), none of which was used for training the MLP classifier. Apparently, the polynomial faulting is depicted well in the time section, whereas the good match in the vertical sections supports the accuracy of the trained MLP classifier in recognizing the faults from the rest of the non-faulting zones in the GSB area.

Applications

We have illustrated the proposed workflow of the super-attribute-based SVM/MLP classification and verified its accuracy in seismic fault detection through applications to the GSB seismic data set. The generated fault volume (Figure 11) is found suitable for further assisting seismic fault interpretation in more ways, such as VFI, seeded fault picking (SFP), and automatic fault extraction (AFE). Considering the overall better performance of the MLP scheme over the SVM one, we use the MLP fault volume (Figure 11b) for demonstrating how the proposed workflow facilitates seismic fault interpretation in the three ways below.

Volumetric fault imaging

VFI is considering one of the most straightforward and convenient approach for fault interpretation by mapping all the faults simultaneously, which requires minimum human interference and thereby successfully avoids interpreter bias. Figure 14a displays the volumetric images of all the potential faults from the GSB data set, which clearly depicts the distribution of the polynomial faulting system. Such a visualization offers a rapid solution for understanding the geologic complexities and investigating the role of each fault in the process of basin evolution from an overall perspective.

Automatic fault extraction

Although imaging all of the potential faults in a 3D seismic data set, VFI fails to interpret each of these faults as an individual object, which is essential for quantitative fault interpretation and structural modeling. AFE is developed for resolving such a limitation, which successfully segments a fault volume into a set of fault patches based on the constraints of a fault surface being planar or slightly bent. Figure 14b displays the fault patches automatically generated from the GSB data set. The AFE algorithm used in this work is provided by Petrel.

Seeded fault picking

Due to the presence of coherence noises (e.g., acquisition footprints) and/or processing artifacts, the AFE results are often less satisfactory in two cases that depend on the parameter configuration (e.g., the minimum pixel number and dipping angle/azimuth). Particularly, using a set of conservative parameters ensures the successful interpretation of the target faults, but some fake faults are generated from noises and artifacts at the same time. On the contrary, artificial lineaments can be significantly avoided by aggressively restraining the parameters, which in turn runs the risk of missing the actual faults of interpretational interest. In addition, in case of a large fault being strongly bent or conical, the AFE tool may split such a fault into several small pieces and extracts them as different patches (B. Payne, personal communication, 2015; Di and Gao, 2017a). For an optimal trade-off between accuracy and artifacts, semiautomatic fault interpretation tools, such as SFP, offer an efficient solution for accurately interpreting the faults of interest while maximally eliminating the introduction of artifacts (Di and AlRegib, 2019). Figure 14c displays the seeded picking of five faults from the GSB data set, with the initial seeds denoted as the black dots.

Discussions

The work proposes retrieving 2D attribute patches of the selected seismic attributes and feeding such super attributes into the SVM and MLP classifiers to help reduce the misclassification of coherent noises and processing artifacts

with distinct reflection patterns. Correspondingly, the retrieval window size and orientation play a key role in controlling the classification accuracy. Particularly,

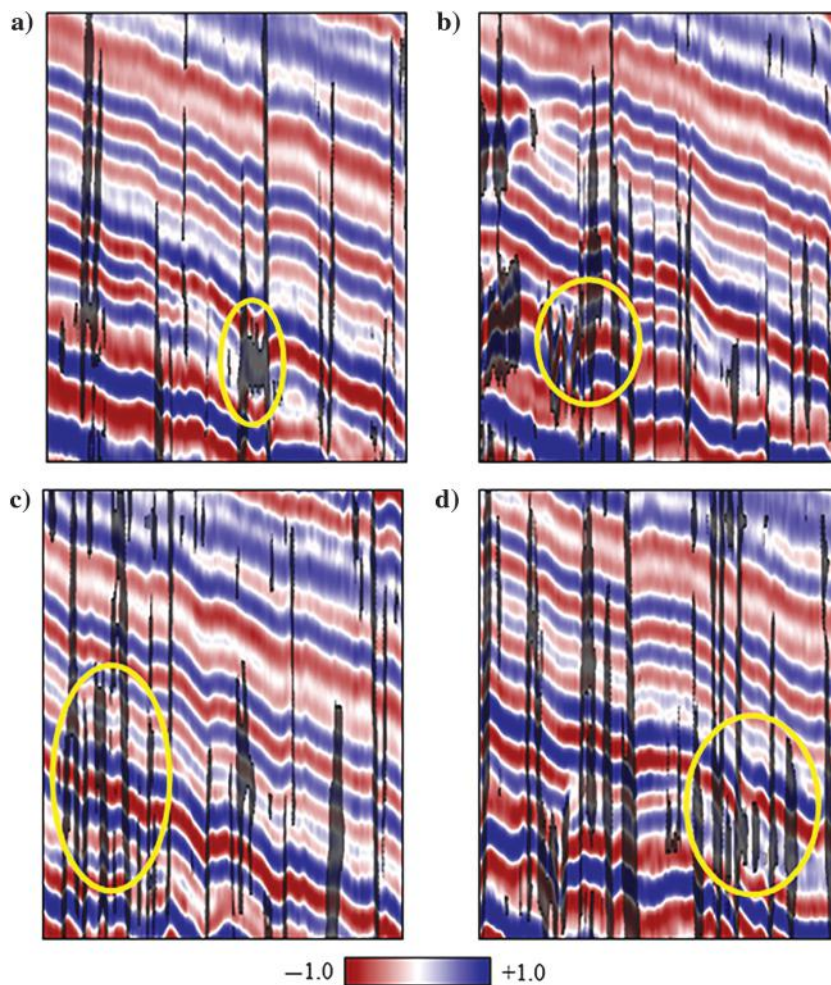


Figure 15. The clipping of the generated fault volume by the 3D super-attribute-based MLP classification to four randomly selected vertical sections, including (a) inline 1791, (b) inline 2011, (c) crossline 2600, and (d) crossline 3000. Notice the improved visualization compared to the maps from the 2D super attributes (Figure 13).

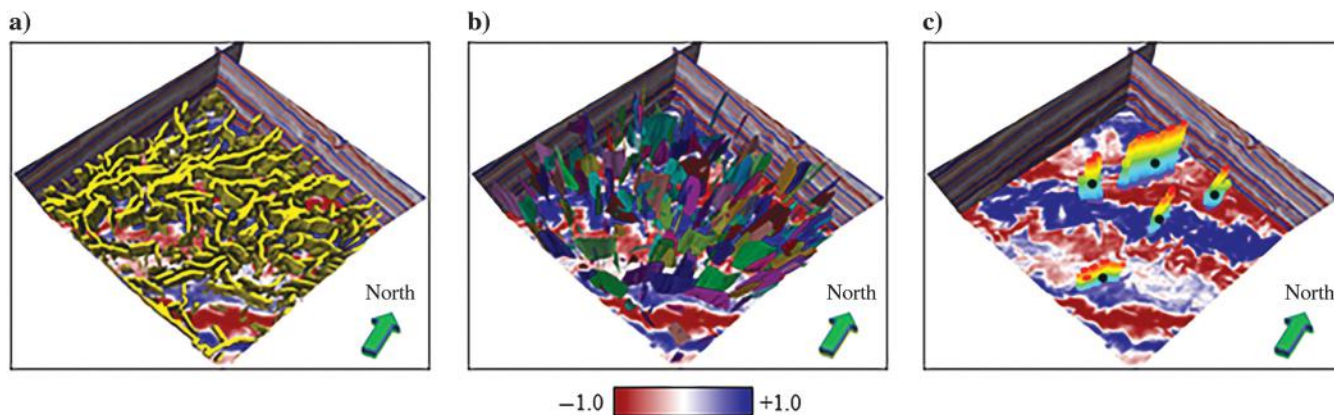


Figure 14. Three applications of the fault volume in the GSB area generated from the proposed super-attribute-based MLP classification, including (a) VFI, (b) AFE, and (c) SFP.

the window size determines how much of the seismic signals is used for defining the fault pattern; therefore, the use of a larger window is capable of utilizing more seismic information and would be more effective in differentiating the noises and artifacts from the true faults, but in turn requires more computational power. Similarly, the orientation of retrieving attribute patches determines how accurate the fault pattern is imaged when

Table 7. The confusion matrix of applying the 3D super-attribute-based MLP classification to the 10 testing sections.

		Prediction	
		Nonfault	Fault
Actual	Nonfault	267,668	56,260
	Fault	1998	16,794

Note the improved overall accuracy and the reduced false-positive rate compared to the 2D super-attribute-based one (Table 4) and the traditional sample-based one (Table 6).

Table 8. The confusion matrix of applying the trained MLP model from the 16 automatically generated CNN attributes to the 10 testing sections.

		Prediction	
		Nonfault	Fault
Actual	Nonfault	262,248	37,744
	Fault	94	18,154

Note the improved overall accuracy and the true-positive rate and the reduced false-positive rate compared to these from the 14 manually selected seismic attributes (Tables 3–7).

it is projected from the 3D to the 2D space. Ideally, the optimal orientation is expected perpendicular to the faults, whereas the fault is indiscernible if the retrieval orientation is parallel to its plane. However, it is challenging and not feasible without a well-documented description of the subsurface structures particularly for seismic data like the GSB data with polynomial faulting. The negative impacts of inappropriate super-attribute retrieval can be eliminated by extending 2D patterns to 3D, so that the faults are defined as close as to the original seismic signals and learned by an ML classifier. Figure 15 displays the corresponding fault detection in the same four vertical sections as shown in Figure 13. Apparently, the images are further cleaned with less noise, if compared to the 2D super-attribute-based results (denoted by the circles in Figure 13). Such improvement is reflected as the lower false positive rate (0.17) in the corresponding confusion matrix (Table 7).

Similar to the traditional multiattribute classification, the accuracy of the proposed SAC also greatly depends on an experienced interpreter in selecting a set of seismic attributes that are indicative of distinguishing faults and the rest of the geologic features (e.g., Barnes and Laughlin, 2002; Di et al., 2017). Ideally, the selected seismic attribute shall be capable of exactly grouping the faults and nonfaults into two separate clusters with a clear boundary between them in the corresponding attribute domain. However, due to the complexities of the subsurface geology and the presence of seismic noise, most seismic attributes fail to serve such a purpose, and overlapping of samples with different labels often occurs as demonstrated in Figure 7, causing the misclassifications shown in Figures 10–15 and Tables 3–7. In addition, with the subsurface geology varying from one study area to another, it is even more challenging for preparing some certain attributes that are applicable to multiple seismic surveys. Therefore,

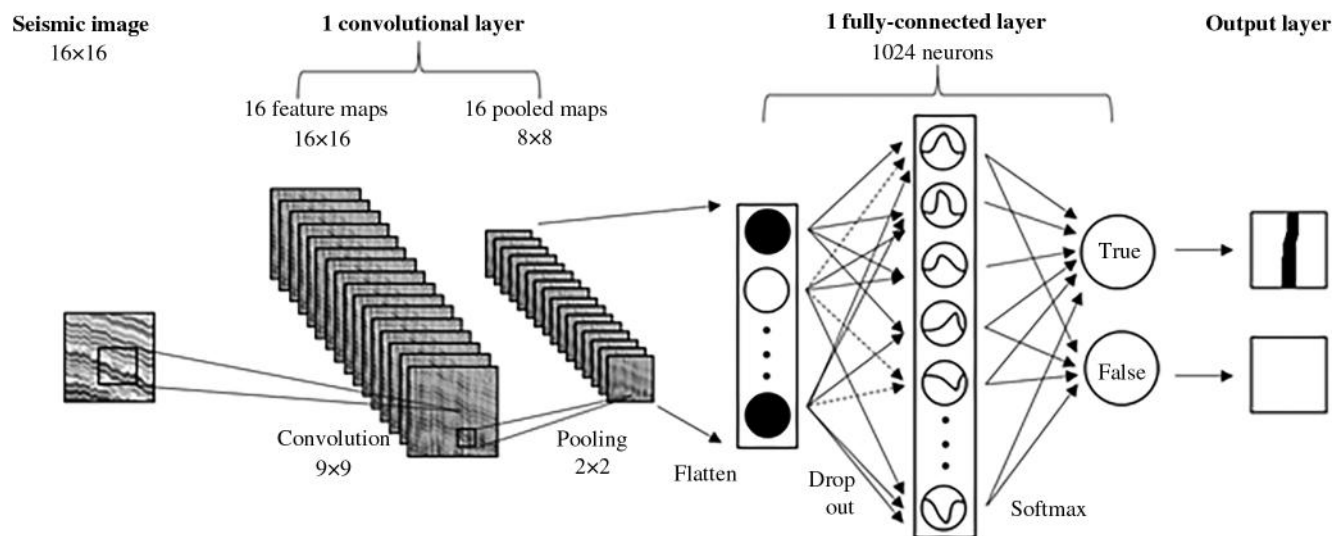


Figure 16. The simple CNN architecture used for investigating automatic attribute extraction in this study.

developing a scheme for automatic seismic attribute selection is of significant importance for improving multi-attribute-based seismic feature interpretation.

Such automatic attribute generation becomes feasible with recent progress in image processing and deep learning, such as the CNN, which first extracts several features from the input seismic images through at least one convolutional layer and then connects the generated features with the labels through an MLP network (Figure 16). Therefore, the convolutional layer(s) can be considered as an adaptive attribute generator, which is capable of generating the most useful attributes, so that maximum classification accuracy would be achieved by the following MLP network. Figure 17 displays the automatically generated 16 attributes from a given seismic images. Compared to these manually selected seismic attributes (Figures 3–5), we notice that the CNN attributes appear only slightly different from the original seismic image and thus are of little physical meaning to interpreters, implying that the convolutional masks are simple in math compared with the existing attribute algorithms (e.g., coherence, curvature, and GLCM). Then, we investigate whether an MLP classifier can parse the automatically generated 16 CNN attributes for fault detection by feeding them into the proposed super-attribute-based MLP classification (Figure 1). Figure 18 displays the clipping of the generated fault volume

to the same four vertical sections as those in Figures 13 and 15, and Table 8 shows the corresponding confusion matrix of applying the CNN attribute-based MLP classification to the 10 testing sections, which demonstrates an improved overall accuracy and true positive rate as well as a reduced false positive rate. Therefore, although the faults remain implicit in each of the CNN features, the following MLP network successfully integrates these implicit attributes and maps them with the fault labels in a more accurate way than the manually selected 14 seismic attributes (Table 1), indicating the feasibility of using the automatically extracted CNN attributes for fault detection.

Finally, the CNN networks have complexities in their architecture and applications, and only the simplest one-layer CNN (Figure 16) is used for automatic attribute extraction in this study. More work is needed in the future for better investigating the impacts of its key hyperparameters (e.g., the number of layers and neurons, size of convolution and pooling, choice of activation functions, and learning rate) on interpreting seismic signals, addressing the commonly occurring issues (e.g., underfitting versus overfitting), and more importantly generating suites of CNN attributes for interpreting the important seismic features and subsurface characteristics (e.g., salt body, depositional facies, and elastic properties).

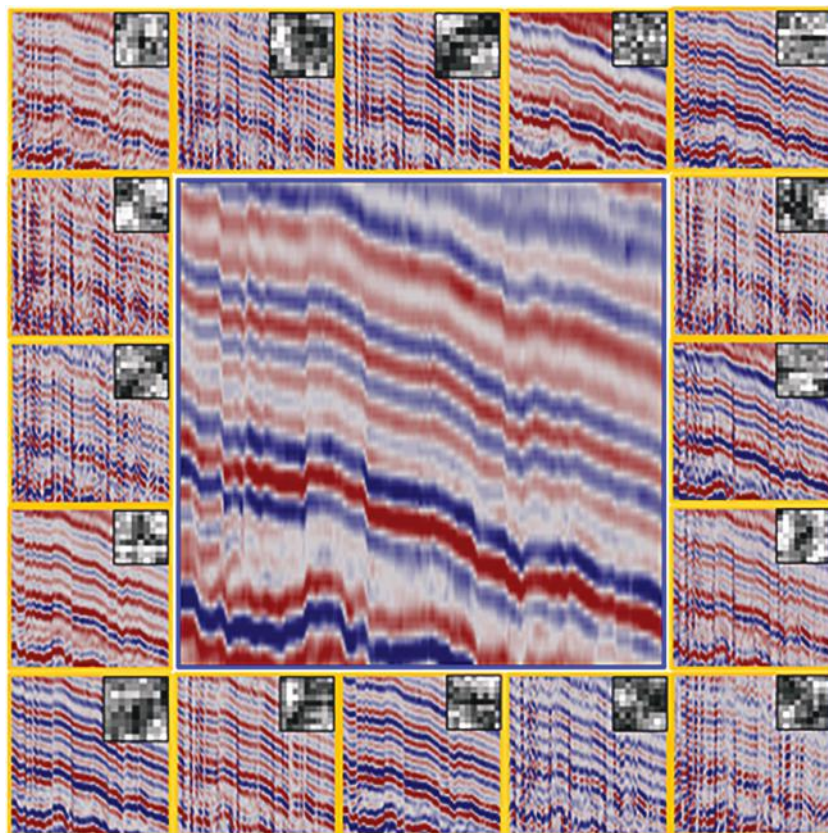


Figure 17. The 16 attributes automatically generated by the one-layer CNN network (Figure 16) for a given seismic image (center), with the corresponding filters on the top-right corner. Note that all of the features appear similar to the original amplitude.

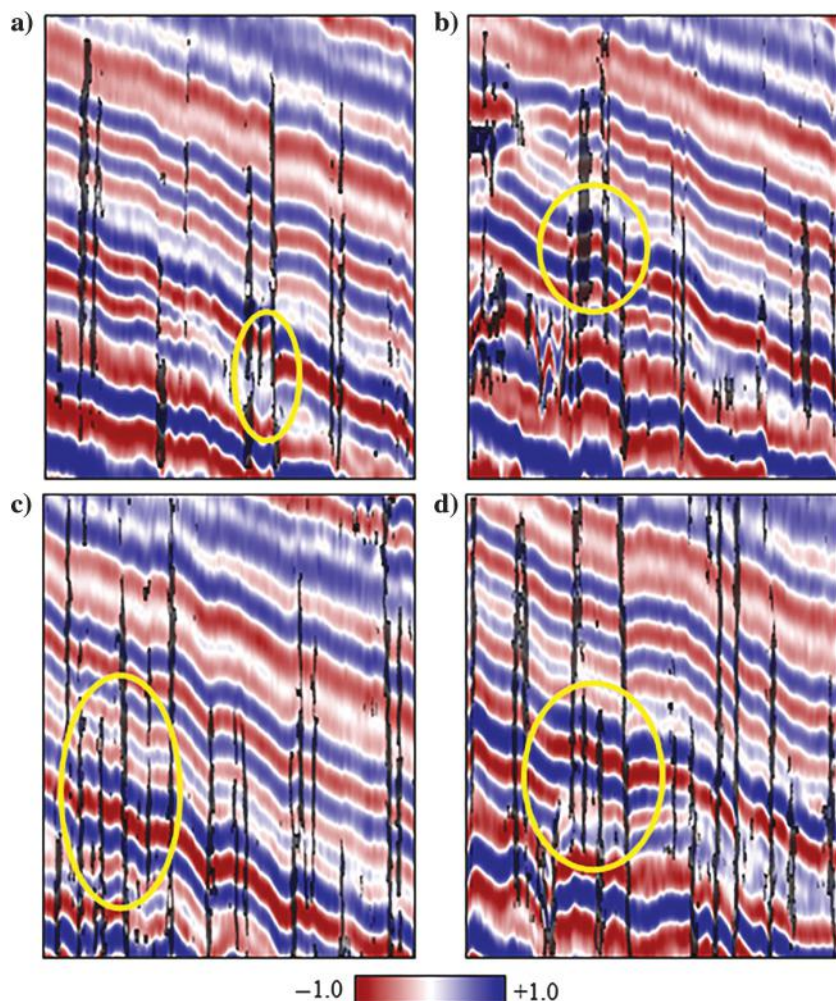


Figure 18. The clipping of the fault volume generated from the 16 CNN attributes to four randomly selected vertical sections, including (a) inline 1791, (b) inline 2011, (c) crossline 2600, and (d) crossline 3000. Notice the improved visualization compared to the maps from the 2D super attributes (Figure 13) and 3D super attributes (Figure 17).

Conclusion

Reliable detection of faults and fractures from 3D seismic data is essential for subsurface interpretation and reservoir characterization. This study has presented an efficient scheme for improving fault interpretation via SAC using the popular SVM and MLP algorithms. Such a workflow is superior over the traditional ones in three aspects. First, the SVM/MLP classifier is computationally efficient in integrating as many attributes as specified by an experienced interpreter, whereas the traditional approaches (e.g., RGB corendering and crossplotting) limit their input to no more than five attributes. Second, the use of super attributes ensures that the machine learning defines, identifies, and learns the target seismic features from the perspective of local seismic patterns, which is more reliable and robust particularly in the presence of seismic noise and processing artifacts with distinct patterns. Third, the implementation of the new scheme requires less on the computer/workstation hardware configuration than the CNN and its derivatives.

Considering the important role of attribute selection in multiattribute-based seismic feature classification, the emerging CNN was also tested for automatic attribute extraction in this study by treating the convolutional layers as an adaptive attribute generator. Such a network is capable of generating a set of simple but helpful attributes to build an optimal mapping relationship between the seismic images and the target labels. More work is in need for in-depth investigating such a network before implementing it for automatic seismic attribute extracting to assist the challenging seismic interpretation tasks, such as salt body delineation and facies analysis.

Acknowledgments

This work is supported by the Center for Energy and Geo Processing at the Georgia Institute of Technology and the King Fahd University of Petroleum and Minerals. Many thanks go to the editors and reviewers for providing insightful suggestions on improving the paper quality. We thank New Zealand Petroleum and Minerals for providing the 3D seismic data set over the GSB. The machine-learning-based classification algorithms are provided by the open-source Python packages Scikit-learn and TensorFlow.

Data and materials availability

Data associated with this research are available and can be accessed via the following URL: <https://haibindi.wixsite.com/haibin-di/software-tools>.

References

- Admasu, F., S. Back, and K. Toennies, 2006, Autotracking of faults on 3D seismic data: *Geophysics*, **71**, no. 6, A49–A53, doi: [10.1190/1.2358399](https://doi.org/10.1190/1.2358399).
- AlBinHassan, N. M., and K. Marfurt, 2003, Fault detection using Hough transforms: 73rd Annual International Meeting, SEG, Expanded Abstracts, 1719–1721, doi: [10.1190/1.1817639](https://doi.org/10.1190/1.1817639).
- Al-Dossary, S., and K. J. Marfurt, 2006, 3D volumetric multi-spectral estimates of reflector curvature and rotation: *Geophysics*, **71**, no. 5, P41–P51, doi: [10.1190/1.2242449](https://doi.org/10.1190/1.2242449).
- Ashbridge, J., C. Pryce, F. Coutel, and M. Welch, 2000, Fault and fracture prediction from coherence data analysis. A case study: The Magnus Field, UKCS: 70th Annual International Meeting, SEG, Expanded Abstracts, 1564–1567, doi: [10.1190/1.1815709](https://doi.org/10.1190/1.1815709).
- Bahorich, M., and S. Farmer, 1995, 3-D seismic discontinuity for faults and stratigraphic features: The coherence

- cube: The Leading Edge, **14**, 1053–1058, doi: [10.1190/1.1437077](https://doi.org/10.1190/1.1437077).
- Barghout, L., 2015, Spatial-taxon information granules as used in iterative fuzzy-decision-making for image segmentation, in W. Pedrycz and S.-M. Chen, eds., *Granular computing and decision-making*: Springer, 285–318.
- Barnes, A. E., 2006, A filter to improve seismic discontinuity data for fault interpretation: *Geophysics*, **71**, no. 3, P1–P4, doi: [10.1190/1.2195988](https://doi.org/10.1190/1.2195988).
- Barnes, A. E., and K. J. Laughlin, 2002, Investigation of methods for unsupervised classification of seismic data: 72nd Annual International Meeting, SEG, Expanded Abstracts, 2221–2224, doi: [10.1190/1.1817152](https://doi.org/10.1190/1.1817152).
- Chopra, S., 2002, Coherence cube and beyond: First Break, **20**, 27–33, doi: [10.1046/j.1365-2397.2002.00225.x](https://doi.org/10.1046/j.1365-2397.2002.00225.x).
- Cohen, I., and R. R. Coifman, 2002, Local discontinuity measures for 3-D seismic data: *Geophysics*, **67**, 1933–1945, doi: [10.1190/1.1527094](https://doi.org/10.1190/1.1527094).
- Cortes, C., and V. Vapnik, 1995, Support-vector networks: *Machine Learning*, **20**, 273–297.
- Crawford, M., and D. Medwedeff, 1999, Automated extraction of fault surface from 3D seismic prospecting data: U.S. Patent 5,987,388.
- Cuingnet, R., C. Rosso, M. Chupin, S. Lehericy, D. Dormont, H. Benali, Y. Samson, and O. Colliot, 2011, Spatial regularization of SVM for the detection of diffusion alterations associated with stroke outcome: *Medical Image Analysis*, **15**, 729–737, doi: [10.1016/j.media.2011.05.007](https://doi.org/10.1016/j.media.2011.05.007).
- Di, H., and G. AlRegib, 2017, Volumetric fault imaging based on seismic geometry analysis: AAPG Annual Convention and Exhibition, Search and Discovery Article #90291.
- Di, H., and G. AlRegib, 2019, Semiautomatic fault/fracture interpretation based on seismic geometry analysis: *Geophysical Prospecting*, **67**, 1379–1391, doi: [10.1111/1365-2478.12769](https://doi.org/10.1111/1365-2478.12769).
- Di, H., and D. Gao, 2014a, Gray-level transformation and Canny edge detection for 3D seismic discontinuity enhancement: *Computers and Geosciences*, **72**, 192–200, doi: [10.1016/j.cageo.2014.07.011](https://doi.org/10.1016/j.cageo.2014.07.011).
- Di, H., and D. Gao, 2014b, A new algorithm for evaluating 3D curvature and curvature gradient for improved fracture detection: *Computers and Geosciences*, **70**, 15–25, doi: [10.1016/j.cageo.2014.05.003](https://doi.org/10.1016/j.cageo.2014.05.003).
- Di, H., and D. Gao, 2016a, Efficient volumetric extraction of most positive/negative curvature and flexure attributes for improved fracture characterization from 3D seismic data: *Geophysical Prospecting*, **64**, 1454–1468, doi: [10.1111/1365-2478.12350](https://doi.org/10.1111/1365-2478.12350).
- Di, H., and D. Gao, 2016b, Improved estimates of seismic curvature and flexure based on 3D surface rotation in the presence of structure dip: *Geophysics*, **81**, no. 2, IM37–IM47, doi: [10.1190/geo2015-0258.1](https://doi.org/10.1190/geo2015-0258.1).
- Di, H., and D. Gao, 2017a, Seismic attribute-aided fault detection in petroleum industry: A review, in D. Martin, ed., *Fault detection: Methods, applications and technology*: Nova Science Publishers, 53–80.
- Di, H., and D. Gao, 2017b, 3D seismic flexure analysis for subsurface fault detection and fracture characterization: *Pure and Applied Geophysics*, **174**, 747–761, doi: [10.1007/s00024-016-1406-9](https://doi.org/10.1007/s00024-016-1406-9).
- Di, H., and D. Gao, 2017c, Nonlinear gray-level co-occurrence matrix texture analysis for improved seismic facies interpretation: *Interpretation*, **5**, no. 3, SJ31–SJ40, doi: [10.1190/INT-2016-0214.1](https://doi.org/10.1190/INT-2016-0214.1).
- Di, H., M. A. Shafiq, and G. AlRegib, 2017, Seismic fault detection based on multi-attribute support vector machine analysis: 87th Annual International Meeting, SEG, Expanded Abstracts, 2039–2044, doi: [10.1190/segam2017-17748277.1](https://doi.org/10.1190/segam2017-17748277.1).
- Di, H., M. A. Shafiq, and G. AlRegib, 2018c, Multi-attribute k-means clustering for salt boundary delineation from 3D seismic data: *Geophysical Journal International*, **215**, 1999–2007, doi: [10.1093/gji/ggy376](https://doi.org/10.1093/gji/ggy376).
- Di, H., Z. Wang, and G. AlRegib, 2018a, Seismic fault detection from post-stack amplitude by convolutional neural networks: 80th Annual International Conference and Exhibition, EAGE, Extended Abstracts, Tu-D-11.
- Di, H., Z. Wang, and G. AlRegib, 2018b, Why using CNN for seismic interpretation? An investigation: 88th Annual International Meeting, SEG, Expanded Abstracts, 2216–2220, doi: [10.1190/segam2018-2997155.1](https://doi.org/10.1190/segam2018-2997155.1).
- Dorn, G. A., 2002, Computing and visualization: The Leading Edge, **21**, 581–586, doi: [10.1190/1.1490638](https://doi.org/10.1190/1.1490638).
- Eichkitz, C. G., J. Amtmann, and M. G. Schreilechner, 2013, Calculation of grey level co-occurrence matrix-based seismic attributes in three dimensions: *Computers and Geosciences*, **60**, 176–183, doi: [10.1016/j.cageo.2013.07.006](https://doi.org/10.1016/j.cageo.2013.07.006).
- Gao, D., 2003, Volume texture extraction for 3D seismic visualization and interpretation: *Geophysics*, **68**, 1294–1302, doi: [10.1190/1.1598122](https://doi.org/10.1190/1.1598122).
- Gao, D., 2013, Integrating 3D seismic curvature and curvature gradient attributes for fracture detection: Methodologies and interpretational implications: *Geophysics*, **78**, no. 2, O21–O38, doi: [10.1190/geo2012-0190.1](https://doi.org/10.1190/geo2012-0190.1).
- Gao, D., and H. Di, 2015, Extreme curvature and extreme flexure analysis for fracture characterization from 3D seismic data: New analytical algorithms and geologic implications: *Geophysics*, **80**, no. 2, IM11–IM20, doi: [10.1190/geo2014-0185.1](https://doi.org/10.1190/geo2014-0185.1).
- Gersztenkorn, A., and K. J. Marfurt, 1999, Eigenstructure-based coherence computations as an aid to 3-D structural and stratigraphic mapping: *Geophysics*, **64**, 1468–1479, doi: [10.1190/1.1444651](https://doi.org/10.1190/1.1444651).
- Gibson, D., M. Spann, J. Turner, and T. Wright, 2005, Fault surface detection in 3-D seismic data: *IEEE Transactions on Geoscience and Remote Sensing*, **43**, 2094–2102, doi: [10.1109/TGRS.2005.852769](https://doi.org/10.1109/TGRS.2005.852769).
- Hale, D., 2013, Methods to compute fault images, extract fault surfaces, and estimate fault throws from 3D seismic images: *Geophysics*, **78**, no. 2, O33–O43, doi: [10.1190/geo2012-0331.1](https://doi.org/10.1190/geo2012-0331.1).

- Huang, L., X. Dong, and T. E. Clee, 2017, A scalable deep learning platform for identifying geologic features from seismic attributes: *The Leading Edge*, **36**, 249–256, doi: [10.1190/tle36030249.1](https://doi.org/10.1190/tle36030249.1).
- Kington, J., 2015, Semblance, coherence, and other discontinuity attributes: *The Leading Edge*, **34**, 1510–1512, doi: [10.1190/tle34121510.1](https://doi.org/10.1190/tle34121510.1).
- Laake, A., 2013, Structural interpretation in color — A new RGB processing techniques for extracting geological structures from seismic data: 83rd Annual International Meeting, SEG, Expanded Abstracts, 1472–1476, doi: [10.1190/segam2013-0079.1](https://doi.org/10.1190/segam2013-0079.1).
- Lavialle, O., S. Pop, C. Germain, M. Donias, S. Guillon, N. Keskes, and Y. Berthoumieu, 2007, Seismic fault preserving diffusion: *Journal of Applied Geophysics*, **61**, 132–141, doi: [10.1016/j.jappgeo.2006.06.002](https://doi.org/10.1016/j.jappgeo.2006.06.002).
- Lee, Y., Y. Lin, and G. Wahba, 2004, Multicategory support vector machines: Theory and application to the classification of microarray data and satellite radiance data: *Journal of the American Statistical Association*, **99**, 67–81, doi: [10.1198/016214504000000098](https://doi.org/10.1198/016214504000000098).
- Lu, P., M. Morris, S. Brazell, C. Comiskey, and Y. Xiao, 2018, Using generative adversarial networks to improve deep-learning fault interpretation networks: *The Leading Edge*, **37**, 578–583, doi: [10.1190/tle37080578.1](https://doi.org/10.1190/tle37080578.1).
- Luo, Y., W. Higgs, and W. Kowalik, 1996, Edge detection and stratigraphic analysis using 3D seismic data: 66th Annual International Meeting, SEG, Expanded Abstracts, 324–327, doi: [10.1190/1.1826632](https://doi.org/10.1190/1.1826632).
- Machado, G., A. Alali, B. Hutchinson, O. Olorunsola, and K. J. Marfurt, 2016, Display and enhancement of volumetric fault images: *Interpretation*, **4**, no. 1, SB51–SB61, doi: [10.1190/TNT-2015-0104.1](https://doi.org/10.1190/TNT-2015-0104.1).
- Marfurt, K. J., R. L. Kirlin, S. L. Farmer, and M. S. Bahorich, 1998, 3-D seismic attributes using a semblance-based coherency algorithm: *Geophysics*, **63**, 1150–1165, doi: [10.1190/1.1444415](https://doi.org/10.1190/1.1444415).
- Meldahl, P., R. Heggland, B. Bril, and P. de Groot, 1999, The chimney cube, an example of semi-automated detection of seismic objects by directive attributes and neural networks — Part 1: Methodology: 69th Annual International Meeting, SEG, Expanded Abstracts, 931–934, doi: [10.1190/1.1821262](https://doi.org/10.1190/1.1821262).
- Odoh, B. I., J. N. Ilechukwu, and N. I. Okoli, 2014, The use of seismic attributes to enhance fault interpretation of OT field, Niger delta: *International Journal of Geosciences*, **5**, 826–834, doi: [10.4236/ijg.2014.58073](https://doi.org/10.4236/ijg.2014.58073).
- Partyka, G., J. Gridley, and J. Lopez, 1999, Interpretational applications of spectral decomposition in reservoir characterization: *The Leading Edge*, **18**, 353–360, doi: [10.1190/1.1438295](https://doi.org/10.1190/1.1438295).
- Pedersen, S. I., T. Randen, L. Sonneland, and Ø. Steen, 2002, Automatic fault extraction using artificial ants: 72nd Annual International Meeting, SEG, Expanded Abstracts, 512–515, doi: [10.1190/1.1817297](https://doi.org/10.1190/1.1817297).
- Qi, X., and K. Marfurt, 2018, Volumetric aberrancy to map subtle faults and flexures: *Interpretation*, **6**, no. 2, T349–T365, doi: [10.1190/TNT-2017-0114.1](https://doi.org/10.1190/TNT-2017-0114.1).
- Roberts, A., 2001, Curvature attributes and their application to 3D interpreted horizons: *First Break*, **19**, 85–100, doi: [10.1046/j.0263-5046.2001.00142.x](https://doi.org/10.1046/j.0263-5046.2001.00142.x).
- Shafiq, M. A., T. Alshaw, Z. Long, and G. AlRegib, 2016, Salsi: A new seismic attribute for salt dome detection: IEEE International Conference on Acoustics, Speech and Signal Processing, 1876–1880.
- Shafiq, M. A., Z. Wang, A. Amin, T. Hegazy, M. Deriche, and G. AlRegib, 2015, Detection of salt-dome boundary surfaces in migrated seismic volumes using gradient of textures: 85th Annual International Meeting, SEG, Expanded Abstracts, 1811–1815, doi: [10.1190/segam2015-5927230.1](https://doi.org/10.1190/segam2015-5927230.1).
- Stark, T., 2006, Visualization techniques for enhancing stratigraphic inferences from 3D seismic data volumes: *First Break*, **24**, 75–85.
- Tingdahl, K. M., and M. de Rooij, 2005, Semi-automatic detection of faults in 3D seismic data: *Geophysical Prospecting*, **53**, 533–542, doi: [10.1111/j.1365-2478.2005.00489.x](https://doi.org/10.1111/j.1365-2478.2005.00489.x).
- van Bemmelen, P. P., and R. E. Pepper, 2000, Seismic signal processing method and apparatus for generating a cube of variance values: U.S. Patent 6,151,555.
- Wang, S., S. Yuan, B. Yan, Y. He, and W. Sun, 2016, Directional complex-valued coherence attributes for discontinuous edge detection: *Journal of Applied Geophysics*, **129**, 1–7, doi: [10.1016/j.jappgeo.2016.03.016](https://doi.org/10.1016/j.jappgeo.2016.03.016).
- Wang, Z., and G. AlRegib, 2014, Automatic fault surface detection using 3D Hough transform: 84th Annual International Meeting, SEG, Expanded Abstracts, 1439–1444, doi: [10.1190/segam2014-1590.1](https://doi.org/10.1190/segam2014-1590.1).
- Wang, Z., Z. Long, G. AlRegib, A. Asjad, and M. A. Deriche, 2014a, Automatic fault tracking across seismic volumes via tracking vectors: IEEE International Conference on Image Processing, 5851–5855.
- Wang, Z., D. Temel, and G. AlRegib, 2014b, Fault detection using color blending and color transformations: IEEE Global Conference on Signal and Information Processing, 999–1003.
- Wu, X., and S. Fomel, 2018, Automatic fault interpretation with optimal surface voting: *Geophysics*, **83**, no. 5, O67–O82, doi: [10.1190/geo2018-0115.1](https://doi.org/10.1190/geo2018-0115.1).
- Wu, X., and D. Hale, 2016, 3D seismic image processing for faults: *Geophysics*, **81**, no. 2, IM1–IM11, doi: [10.1190/geo2015-0380.1](https://doi.org/10.1190/geo2015-0380.1).
- Wu, X., L. Liang, Y. Shi, and S. Fomel, 2019, FaultSeg3D: Using synthetic datasets to train an end-to-end convolutional neural network for 3D seismic fault segmentation: *Geophysics*, **84**, no. 3, IM35–IM45, doi: [10.1190/geo2018-0646.1](https://doi.org/10.1190/geo2018-0646.1).
- Xiong, W., X. Ji, Y. Ma, Y. Wang, N. M. AlBinHassan, M. N. Ali, and Y. Luo, 2018, Seismic fault detection with convolutional neural network: *Geophysics*, **83**, no. 5, O97–O103, doi: [10.1190/geo2017-0666.1](https://doi.org/10.1190/geo2017-0666.1).

- Yu, J., 2014, Using cylindrical surface-based curvature change rate to detect faults and fractures: *Geophysics*, **79**, no. 5, O1–O9, doi: [10.1190/geo2014-0003.1](https://doi.org/10.1190/geo2014-0003.1).
- Zhang, B., Y. Liu, M. Pelissier, and N. Hemstra, 2014, Semi-automated fault interpretation based on seismic attributes: *Interpretation*, **2**, no. 1, SA11–SA19, doi: [10.1190/INT-2013-0060.1](https://doi.org/10.1190/INT-2013-0060.1).
- Zhao, T., V. Jayaram, A. Roy, and K. J. Marfurt, 2015, A comparison of classification techniques for seismic facies recognition: *Interpretation*, **3**, no. 4, SAE29–SAE58, doi: [10.1190/INT-2015-0044.1](https://doi.org/10.1190/INT-2015-0044.1).
- Zhao, T., and P. Mukhopadhyay, 2018, A fault-detection workflow using deep learning and image processing: 88th Annual International Meeting, SEG, Expanded Abstracts, 1966–1970, doi: [10.1190/segam2018-2997005.1](https://doi.org/10.1190/segam2018-2997005.1).
- Zheng, Z., P. Kavousi, and H. Di, 2014, Multi-attributes and neural network-based fault detection in 3D seismic interpretation: *Advanced Materials Research*, **838–841**, 1497–1502, doi: [10.4028/www.scientific.net/AMR.1065-1069](https://doi.org/10.4028/www.scientific.net/AMR.1065-1069).

Biographies and photographs of the authors are not available.